ENVIRONMENTAL RESEARCH

LETTERS

LETTER • OPEN ACCESS

Linking repeat lidar with Landsat products for large scale quantification of fire-induced permafrost thaw settlement in interior Alaska

To cite this article: Caiyun Zhang et al 2023 Environ. Res. Lett. 18 015003

View the article online for updates and enhancements.

You may also like

- Reorganization of vegetation, hydrology and soil carbon after permafrost degradation across heterogeneous boreal landscapes
 M Torre Jorgenson, Jennifer Harden,
- M Torre Jorgenson, Jennifer Harden Mikhail Kanevskiy et al.
- Impact of fire on global land surface air temperature and energy budget for the 20th century due to changes within ecosystems
- ecosystems
 Fang Li, David M Lawrence and Ben
 Bond-Lamberty
- Trends in tree cover change over three decades related to interannual climate variability and wildfire in California Francis K Dwomoh, Roger F Auch, Jesslyn F Brown et al.

ENVIRONMENTAL RESEARCH

LETTERS



OPEN ACCESS

RECEIVED

17 July 2022

REVISED

6 December 2022

ACCEPTED FOR PUBLICATION

15 December 2022

PUBLISHED

3 January 2023

Original content from this work may be used under the terms of the Creative Commons Attribution 4.0 licence.

Any further distribution of this work must maintain attribution to the author(s) and the title of the work, journal citation and DOI.



LETTER

Linking repeat lidar with Landsat products for large scale quantification of fire-induced permafrost thaw settlement in interior Alaska

Caiyun Zhang^{1,*}, Thomas A Douglas², David Brodylo¹ and M Torre Jorgenson³

- Department of Geosciences, Florida Atlantic University, Boca Raton, FL 33431, United States of America
- ² U.S. Army Cold Regions Research & Engineering Laboratory, Fort Wainwright, AK 99703, United States of America
- ³ Alaska Ecoscience, Fairbanks, AK 99709, United States of America
- * Author to whom any correspondence should be addressed.

E-mail: czhang3@fau.edu

Keywords: repeat lidar, permafrost, wildfires, machine learning modeling, thaw settlement Supplementary material for this article is available online

Abstract

The permafrost–fire–climate system has been a hotspot in research for decades under a warming climate scenario. Surface vegetation plays a dominant role in protecting permafrost from summer warmth, thus, any alteration of vegetation structure, particularly following severe wildfires, can cause dramatic top–down thaw. A challenge in understanding this is to quantify fire-induced thaw settlement at large scales (>1000 km²). In this study, we explored the potential of using Landsat products for a large-scale estimation of fire-induced thaw settlement across a well-studied area representative of ice-rich lowland permafrost in interior Alaska. Six large fires have affected \sim 1250 km² of the area since 2000. We first identified the linkage of fires, burn severity, and land cover response, and then developed an object-based machine learning ensemble approach to estimate fire-induced thaw settlement by relating airborne repeat lidar data to Landsat products. The model delineated thaw settlement patterns across the six fire scars and explained \sim 65% of the variance in lidar-detected elevation change. Our results indicate a combined application of airborne repeat lidar and Landsat products is a valuable tool for large scale quantification of fire-induced thaw settlement.

1. Introduction

Fire is the largest driver shaping the diverse boreal ecosystems in interior Alaska where \sim 40% is underlain by ice-rich permafrost (Jorgenson *et al* 2022). Effects of wildfires on permafrost such as active layer thickness and thermokarst development are well documented (e.g. Jorgenson *et al* 2010, Brown *et al* 2015, Douglas *et al* 2015, Jones *et al* 2015, Minsley *et al* 2016), and recently reviewed by Holloway *et al* (2020) and Li *et al* (2021). The mechanisms of fire in changing permafrost ecosystems have been recognized: severe wildfire removes the vegetation and surface soil organic matter, and the loss of this insulation increases the ground heat flux and promotes permafrost thaw. In areas of ice-rich permafrost, thaw

triggers ground subsidence and thermokarst development, leading to surface water inundation, vegetation shifts, changes in soil carbon balance and carbon emissions, that can provide positive feedback to climate warming (Douglas *et al* 2014). Recent research of the role of fire in permafrost landscapes has focused on determining which variables control post-fire permafrost behavior, the interactive effects of fire and climate on permafrost degradation and resilience, and modeling and predicting post-fire resilience (Holloway *et al* 2020).

Research interest in the permafrost-fire-climate system has been growing. Current and future projected increases in mean annual air temperature, the length of the summer growing season, and the severity and extent of wildfire are expected to lead to an

increasingly dominant role of wildfire in permafrost ecosystems (Gibson et al 2018). One challenge in understanding this system is to quantify fire-induced thaw settlement which is a gentle and continuous ground subsidence as the ice melts and the active layer deepens downward into near-surface permafrost (Anders et al 2020). Thaw settlement is difficult to measure as there are often no absolute reference frames to compare to the subtle but widespread topographic change in permafrost landscapes (Anders et al 2020). Mapping fire-induced thaw settlement is critical as it is associated with subsequent thermokarst development, snow accumulation, hydrology, vegetation shifts, and commensurate changes in the land-atmospheric exchange of water, energy, and greenhouse gases. Efforts have been made to estimate fire-induced permafrost thaw settlement using spaceborne interferometric synthetic aperture radar (InSAR) techniques (Liu et al 2014, Molan et al 2018, Michaelides et al 2019, Yanagiya and Furuya 2020). Constraints of InSAR for such applications include interferometric phase decorrelation (Antonova et al 2018), and loss of image coherence across large areas within a burn (Jones et al 2015).

Airborne lidar is so far the best technique to generate accurate and fine resolution (<5 m) digital elevation models (DEMs) for a variety of terrestrial applications (Dong and Chen 2018). The application of lidar for cryospheric studies has been increasing but has been limited in permafrost landscapes (Bhardwaj et al 2016). Ideally, repeat lidar measurements can accurately estimate and map thaw settlement with a fine resolution, which is evidenced by Jones et al (2013), Jones et al (2015), Douglas et al (2021) and Rodenhizer et al (2022). However, repeat lidar has been seldom applied to quantify elevation changes in fire-influenced permafrost terrains. This is attributable to the high cost for lidar data acquisition, and a limited spatial coverage of airborne platforms compared to the spaceborne sensors. Chasmer and Hopkinson (2017) applied repeat lidar to characterize permafrost loss. The work from Jones et al (2015) is the only effort analyzing post-fire repeat lidar for detecting subsidence caused by the 2007 Anaktuvuk River tundra fire which burned ∼1000 km² in northern Alaska. Multi-temporal lidar is a useful means detecting fire-induced terrain subsidence and thermokarst development since it allows for a direct measure of land surface elevation relative to a geodetic reference frame. Lidar-detected subsidence is highly related to Landsat-derived differenced Normalized Burn Ratio (dNBR), and the trend of post-fire multispectral indices such as Normalized Difference Vegetation Index (NDVI) and Normalized Difference Moisture Index (NDMI) (Jones et al 2015). dNBR is a variable developed from adjacent pre-fire and post-fire optical imagery to estimate

burn severity, which plays a critical role in postfire permafrost degradation and resilience (Keeley 2009). Multispectral indices NDVI and NDMI indicate vegetation succession, which is coupled with topographic change, and other interactions in post-fire permafrost environments. A linkage of repeat lidar with optical satellite sensors like Landsat through modern machine learning modeling techniques may provide potential for large-scale quantification of fire-induced thaw settlement across broader, recently burned regions, as well as other historic fires.

The Tanana Flats (\sim 2500 km²), a representative lowland landscape south of Fairbanks in interior Alaska, consists of a complex mosaic of ice-rich permafrost and permafrost free ecosystems. The region is a hotspot for thermokarst, and ground collapse caused by thawing permafrost (Jorgenson et al 2020, 2022). Much of the land is part of a military training area managed by the U.S. Department of Defense. In the past two decades, six large fires with burn scars larger than 20 km² have occurred and influenced a total of 1250 km² (\sim 50%) across this training area. The large scale effects of these fires on land cover change, post-fire resilience, and subsequent thaw settlement remain unknown, although analyses using data collected along several transects have revealed fire-induced permafrost degradation over this area (Brown et al 2015, Douglas et al 2015). To further understand the effects of disturbance from fires and climate warming on the Tanana Flats training site, the U.S. Army Corps of Engineers (USACE) Cold Regions Research and Engineering Laboratory coordinated the collection of airborne repeat lidar that partly overlapped with the fire scars. This provides a unique opportunity to quantify fire-induced thaw settlement and assess the capacity of operational Landsat products for characterizing fire-influenced permafrost terrains.

In this study, we systematically analyzed the effects of six large fires that occurred since 2000 on the Tanana Flats lowland on land cover change, vegetation dynamics and terrain subsidence, and for the first time developed a machine learning based ensemble approach to quantifying fire-induced thaw settlement across the entire Tanana Flats by linking limited repeat lidar measurements with Landsat products. We assessed three commonly used machine learning algorithms including artificial neural network (ANN), support vector machine (SVM) and random forest (RF) for fire-induced thaw settlement modeling. Machine learning has been extensively applied for modeling in geosciences as reviewed by Dramsch (2020) and Sun et al (2022). Our logic is that each algorithm has its pros and cons, and an ensemble analysis (EA) of comparative models can produce a more robust estimation than the application of a single model. In addition, a spatial uncertainty map can be

created based on analyses of multiple model outputs to complement the traditional statistical error metrics (Zhang *et al* 2022). The specific objectives were to: (a) characterize the response of vegetation to fires using time-series Landsat products; (b) analyze repeat lidar-derived elevation changes related to vegetation shift and burn severity; (c) assess the performance of machine learning algorithms for upscaling lidar-detected permafrost thaw settlement; and (d) identify fire-induced subsidence patterns across the Tanana Flats lowland.

2. Study area, data, and fire history

The Tanana Flats lowland in interior Alaska is underlain by discontinuous permafrost (figure 1). It is situated in a large, abandoned floodplain and alluvial fan, and receives deposits from the fluvial and glaciofluvial sediments of the Alaska Range to the south (Jorgenson et al 1999). Tanana Flats has a gentle elevation gradient of approximately 1 m km⁻¹ declining from southeast to northwest. The Tanana River, the largest tributary of the Yukon River, forms the boundary around the northern portion of Tanana Flats. Land cover types include evergreen forest (spruce), deciduous forest (birch), shrubland, fen, bog, streams, and open water bodies. Field photos of the major land cover types are provided in Figure SI1. Forests are generally located on ice-rich permafrost plateaus elevated above fens and bogs formed in thermokarst depressions. Approximately 50% of this area is in some stage of permafrost degradation caused by fires and climate warming (Jorgenson et al 1999). The climate in interior Alaska is continental, with annual mean precipitation of 28 cm, a typical annual snowfall of 1.7 m, and a wide variation of seasonal mean air temperature ranging from -40 °C in winter to 25 °C in summer.

Data used in this study include historical fire perimeters from the Alaska Interagency Coordination Center (AICC), Landsat derived dNBR products from the National Aeronautics and Space Administration (NASA)'s Arctic-Boreal Vulnerability Experiment (ABoVE, Goetz et al 2022) (Loboda et al 2018), Landsat derived annual dominant land cover across the ABoVE core domain, 1984-2014 (Wang et al 2019), Landsat 8 Collection 2 Level 2 surface reflectance products from the U.S. Geological Survey (USGS) Earth Explorer, and airborne repeat lidar measurements in 2014 and 2020 for USACE. The USACE contracted with the Quantum Spatial Incorporated (Anchorage, Alaska) for lidar data collection using a Lecia ALS80 laser system to yield an average pulse density of ≥ 25 points m⁻² over the targeted lidar survey area (\sim 40 km², figure 1(b)). The vendor processed the lidar point cloud data and generated a 0.25 m hydro-flattened DEM product. The hydroflattening process eliminated artifacts in the digital terrain caused by both increased variability in ranges

or dropouts in laser returns due to the low reflectivity of water. However, limited water bodies appeared in our study area, and they were not within the fire scars. The 2014 lidar was collected on May 9–11, and 2020 lidar was acquired on May 17–18, in a period of 95% snowmelt with leaf-off conditions.

Six major fires occurred since 2000 including the 2001 Survey Line Fire (472 km²), 2004 Willow Creek Fire (28 km²), 2009 Wood River 1 Fire (507 km²), 2010 Willow Creek Fire (56 km²), 2011 Bonnifield 1 Fire (35 km²), and 2012 Dry Creek Fire (191 km²) (figure 1). Partial scar of the 2001 fire and the complete scar of 2004 fire were reburned by the 2009 fire. Examples of field photos of burns and vegetation changes after fires 2001 and 2010 are provided in figure SI2. Because the latest big fire occurred in 2012, we selected six snow and cloud free Landsat 8 scenes after 2012 and calculated annual time series NDVI for modeling. These were collected on 06/18/2013, 08/08/2014, 07/12/2016, 06/13/2017, 07/05/2019, and 07/01/2021, respectively. Landsat 5 and 7 data products were also available following some fires but were not used in this study to reduce uncertainties of reflectance difference across Landsat sensors (Flood 2014, Roy et al 2016). Landsat 8 products are only available since 2013.

3. Methodology

To examine the response of vegetation to fires, we selected land cover data for years 2000, 2002, 2008 and 2014 from NASA's ABoVE annual dominant land cover products and calculated the gain and loss of major land cover classes caused by the six fires. The change between 2000 and 2002 could illustrate the disturbance from the 2001 fire, change between 2002 and 2008 could reveal the effects from the 2004 fire, while change between 2008 and 2014 could document the combined influence from four fires between 2009 and 2012. We selected the dNBR data for each fire from NASA's ABoVE dNBR product and subset it to the fire scar defined by the AICC fire perimeter dataset. We mosaiced the dNBR for the entire Tanana Flats to be used for model development and analysis. We used the dNBR from the first fire that occurred for the reburned areas where a larger dNBR was observed from the first fire than the second fire because the first fire had burned down the vegetation. We calculated time-series NDVI from the selected Landsat 8 surface reflectance datasets, and similarly calculated NDMI to assess its contribution for estimating fire-induced thaw settlement.

To examine the capacity of Landsat products for upscaling thaw settlement detected by repeat lidar data, we developed an object-based machine learning ensemble approach that has proven powerful for thaw depth and snow depth estimation in permafrost ecosystems of interior Alaska using optical imagery and lidar DEMs (Douglas and Zhang 2021,

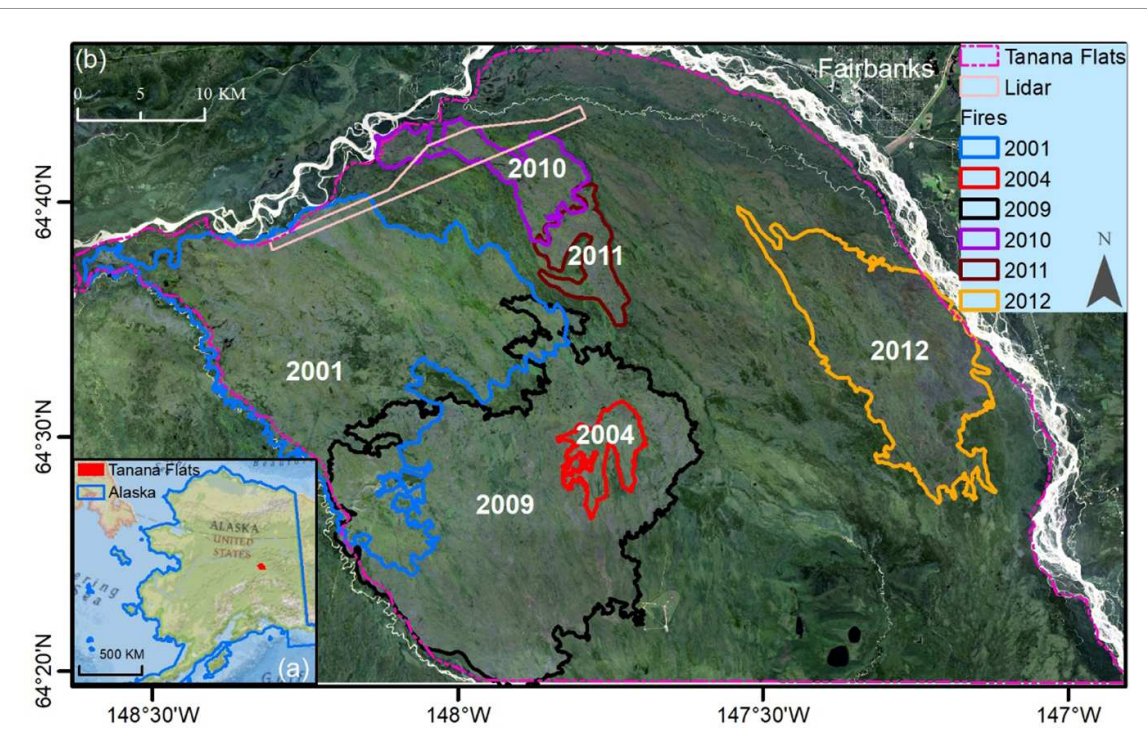


Figure 1. Study area in (a) interior Alaska. (b) Tanana Flats shown in a natural color composite of Landsat 8 imagery collected on 08/08/2014 along with the perimeters of six major fires, and the location of repeat lidar surveys conducted in 2014 and 2020.

Zhang et al 2021). We first determined the lidardetected subsidence by analyzing the errors from lidar measurements (section 3.1), and then linked the detected subsidence with Landsat-derived reflectance, dNBR, and spectral indices at the object level to identify a quantitative relation between the target variable (subsidence) and predictors (Landsat variables) using machine learning regression algorithms. The models were assessed using traditional error metrics including correlation coefficient (r), mean absolute error (MAE), and root mean square error (RMSE). If the models were comparable, we applied a weighted ensemble approach to combine the outputs from multiple models to make the prediction more robust (section 3.3.2). Major steps for upscaling lidardetected subsidence include determination of thaw settlement using repeat lidar, object-based data processing, machine learning ensemble model development, assessment, and mapping applications. They are described below.

3.1. Thaw settlement detection using repeat lidar

Lidar DEMs have errors which should be considered because they will propagate into the DEM of difference (DoD) for elevation change analysis (Wheaton et al 2010). Based on the vendor's 2014 lidar report, the accuracy of the lidar DEM was assessed based on a total of 183 ground control points (GCPs) measured using real time kinematic and post processed kinematic techniques across five land cover classes defined by the USGS: mixed forest, grasslands/herbaceous, shrubland, wetlands, and barren. Lidar data vertical accuracy was reported using the fundamental

vertical accuracy designed to meet guidelines in Federal Geographic Data Committee National Standard for Spatial Data Accuracy. A summary of the lidar accuracy is listed in table 1. For the 2020 lidar, the vendor only reported errors for vegetated area (23.2 cm) and non-vegetated area (5.1 cm) but did not provide errors for each land cover class. Since both 2014 and 2020 lidar data were collected by the same vendor using the same laser system, similar settings, and time (May 2014 and 2020), we thus used the 2014 reported errors in this study. Connecting this error table with the 2014 land cover dataset, we developed an error layer and calculated the propagated error in DoD using an equation revised from Wheaton *et al* (2010) as below:

$$\delta U_{\text{DoD}} = \sqrt{\delta Z_{2020}^2 + \delta Z_{2014}^2} \tag{1}$$

where $\delta U_{\rm DoD}$ is the propagated error in DoD, and $\delta Z_{\rm 2020}$ and $\delta Z_{\rm 2014}$ are individual errors in 2020 DEM and 2014 DEM, respectively. Since we assumed 2020 and 2014 had the same errors across the eight land cover classes appeared in the burned areas, these two variables used the same values in table 1. We selected the conservative 95th percentile error for each land cover class defined by the ABoVE 10-class classification system for the burned areas (table 1) to calculate the accumulative error. Any elevation changes in DoD (|2020 DEM minus 2014 DEM|) less than $\delta U_{\rm DoD}$ were considered noise and dropped in further analysis. The repeat lidar measurements within the unburned areas and the 2001 fire was also dropped

Table 1. Lidar DEM error (cm) in terms of mean, STD 1σ), RMSE, 95th percentile, and the number of GCPs used to assess the vertical accuracy for each land cover class within the fire scars.

Land cover	Mean	STD	RMSE	95th percentile	Number of GCPs
Evergreen forest	1.0	5.5	5.5	8.9	42
Deciduous forest	1.0	5.5	5.5	8.9	
Shrubland	1.3	6.1	6.1	11.3	39
Herbaceous	2.9	2.9	4.0	6.7	17
Sparse vegetation	0.4	3.0	3.0	6.4	57
Barren	0.4	3.0	3.0	6.4	
Fen	3.8	5.7	6.8	12.8	28
Bog	3.8	5.7	6.8	12.8	

because our interest was fire effects and the large time gap between the 2001 fire and the 2014 lidar acquisition. Therefore, lidar detected subsidence over the 2010 fire was analyzed and used for model development. The mean and standard deviation (STD) of $\delta U_{\rm DoD}$ across the 2010 fire was 13.6 cm and 3.3 cm, and about 45% were dropped based on the threshold method.

3.2. Object-based data processing

The object-based image analysis (OBIA) segments imagery into relatively homogeneous objects. It is more accurate than the pixel-based analysis because an object is more representative than any pixels within this object and using the spectral mean of an object in a model can reduce the local spectral noise/variance caused by surrounding pixels (Dronova 2015). We selected the OBIA in the upscaling and generated image objects from the 2014 Landsat imagery using the multiresolution segmentation algorithm in eCognition Developer 10.0 (Trimble 2020). This algorithm starts with a 1 pixel image segment and merges neighboring segments together until a heterogeneity threshold is reached. A challenge using OBIA is to select an appropriate scale parameter given its effects on modeling and mapping results. We applied the commonly used 'trial-and-error' approach to select an optimal scale parameter. We selected the 2014 imagery to generate objects because lidar data was collected in 2014 and no snow and cloud free imagery was available for 2020. Following segmentation, we extracted the spectral mean for each object, and calculated two spectral indices NDVI and NDMI. We also calculated annual time-series NDVI for each object to examine their contribution in thaw settlement estimation. Landsat 8 images collected during 2013–2021 for time series NDVI calculation were provided in section 2. The mean lidar-detected subsidence was calculated for objects where lidar measurements were available, which was spatially matched to Landsat variables at the object level for model development. In total, we obtained 284 matched objects across different land cover types with varying burn severity, which were used for training and testing the model.

3.3. Machine learning ensemble modeling, mapping, and accuracy assessment

3.3.1. Machine learning modeling

Our preliminary analysis showed that the relation of subsidence and Landsat predictors was nonlinear due to the complicated post-fire permafrost response. Machine learning algorithms are valuable in quantifying the nonlinear relation and thus were explored. We selected three popular machine learning algorithms, ANN, SVM and RF, for subsidence modeling based on an exploration of many algorithms integrated in the open-source machine learning software package Waikato Environment for Knowledge Analysis (WEKA) (Hall et al 2009). ANN is a sophisticated machine learning algorithm that has been widely applied in remote sensing classification, as reviewed by Mas and Flores (2008). We selected the commonly used multilayer perceptron method which sets up multiple layers connected by weights to train a model in a nonlinear manner. This algorithm needs to set the number of hidden layers, learning rate and the number of training cycles. SVM is a popular approach (Vapnik 1995) which has also been broadly used in remote sensing, as reviewed by Mountrakis et al (2011). In SVM, parameters including a kernel to be used, precision and penalty need to be specified. RF is a tree-based ensemble approach that constructs numerous small regression trees contributing to the predictions (Breiman 2001), as reviewed by Belgiu and Drãguţ (2016) for remote sensing applications. Two parameters need to be defined in RF: the number of decision trees to create and the number of randomly selected variables considered for splitting each node in a tree. We tuned each model using the experimenter function in WEKA which can determine the best model by setting different parameter through a cycling procedure.

3.3.2. Ensemble estimation for mapping thaw settlement

Each algorithm has its pros and cons, and these algorithms may generate similar accuracy in terms of reference samples but different predictions across a large area. An EA of comparative models can produce a more robust estimation than the application of a single model. In addition, the application of multiple models can generate a spatial uncertainty map to complement the traditional statistical metrics used for error analysis (Zhang *et al* 2021, 2022). We used a weighted combining scheme developed by Zhang *et al* (2018) based on r derived from each model to integrate predictions from different models. If model i (i = 1, 2, ... M) has a correlation coefficient r_i , then the final prediction of subsidence S is calculated as:

$$S = \sum \frac{r_i S_i}{\sum_{i=1}^{M} r_i} \tag{2}$$

where S_i is the prediction from model i, and M is the total number of models in the EA. In this way, a model with a larger r obtains a higher weight, and the sum of weights is 1.0. To make the prediction more robust, at least two models which voted subsidence (negative elevation change) were combined for estimation.

3.3.3. Model accuracy assessment and uncertainty mapping

We applied the commonly used k-fold cross validation method to calibrate and validate each algorithm. The k-fold cross validation randomly splits the reference samples into k equal groups, and then iterates the model k times. In each iteration, one group is used to assess the model, and the remaining k-1 groups are used to train the model. In this way it can avoid over-fitting issues if the same dataset is used for both training and testing. We set k to 10, a common value used in literature. Setting of k was detailed in Anguita et al (2012). After the iteration, prediction was generated for each matched sample and could be used to evaluate model performance by calculating statistical metrics including r, MAE, and RMSE. If EA is used for predicting subsidence, the STD of multiple model outputs to the ensemble prediction (here after referring to as STDE) can be calculated to map the uncertainty in prediction caused by the application of different models. STDE is calculated as:

$$STDE = \sqrt{\frac{\sum_{i=1}^{M} (S_i - S)^2}{M}}$$
 (3)

where S_i , S, and M are same variables as in equation (2).

4. Results

4.1. Burn severity, vegetation change, and lidar-detected subsidence

The mosaiced burn severity quantified by the dNBR across the six fires is displayed in figure 2(a), and land cover types in 2014 (post-fire) and 2000 (pre-fire) are displayed in figures 2(b) and (c). The total coverage, and percentage of major land cover types in 2000, 2002, 2008 and 2014 across the entire Tanana Flats, and areas associated with fires were calculated and summarized in table SI1 and illustrated in figure 3.

Burn severity was heterogeneous within a fire scar and across the six fire scars. The blank stripes in the dNBR map were caused by the lack of data from Landsat 7 due to the failure of Scan Line Corrector after 31 May 2003 in the dNBR dataset (Loboda et al 2018). In terms of the burn severity levels defined by the USGS and the 2000 land cover map, we analyzed areas with dNBR larger than 100 (totaling 842 km²) for each major land cover within the AICC fire perimeters (table SI2). The greatest damage occurred in evergreen forest which accounted for 80% on the affected area. Fen was the second largest ecosystem associated with burned areas, but we attribute the burn estimates to problems with classifying land cover and burn severity in fens rather than to fires. Fen was reported to have the lowest user's accuracy (61%) among the identification of ten classes in NASA ABoVE annual dominant land cover product (Wang et al 2019).

The change between the land cover maps in 2000 and 2014 further illustrated the fire effects on the evergreen forest which covered 1177 km² (46.5% of the area) in 2000 before the six fires but was reduced to 775 km² in 2014 as the result of 2001 fire burned \sim 120 km², the 2004 fire burned \sim 50 km², the 2009– 2012 fires burned \sim 230 km². In total, \sim 400 km² (57%) of the Evergreen Forest within the fire perimeter was affected. Deciduous forest covered \sim 7.8% of the area in 2000 and was reduced by only 0.8% after fires. Fires resulted in the expansion of Shrubland from a pre-fire areal extent of 548 km² (21.6%) to a post-fire areal extent of 720 km² (28.4%). This expansion is distinct across the 2001 fire scar (figures 2(b) and (c)) and better evidenced by the increase of \sim 144 km² between 2000 and 2008, but only \sim 28 km² between 2008 and 2014. This indicates that it might take more than 6 years for a complete encroachment of shrubs after a fire. The expansion of shrubs in the 2009 fire is also clear. The removal of vegetation by fires was also illustrated by the large increase in sparse vegetation defined as areas with 20%-50% vegetation coverage (Wang et al 2019) from 15 km² (0.6%) to a post-fire areal extent of 296 km² (11.7%). Fens covered ~23% of Tanana Flats and were reduced by 2.6% after fires. The decrease in fens, however, is inconsistent with observations that wet, herbaceous fens do not burn and the reported increase in fens from permafrost degradation (Jorgenson et al 2020). The change, again, was more likely due to difficulties in classifying fens with seasonally variable water levels and herbaceous cover.

Figure 4 shows the lidar DoD and detected thaw settlement between 2014 and 2020 over the 2010 fire scar. The elevation change was heterogeneous varying from increase to decrease (figure 4(a)). Here we only focused on thaw settlement analyses after dropping areas with an accumulative error larger than DoD (figure 4(b)). For the burned areas with dNBR larger than 100, repeat lidar analyses revealed a mean elevation decrease of 18.4 cm in evergreen forest with a

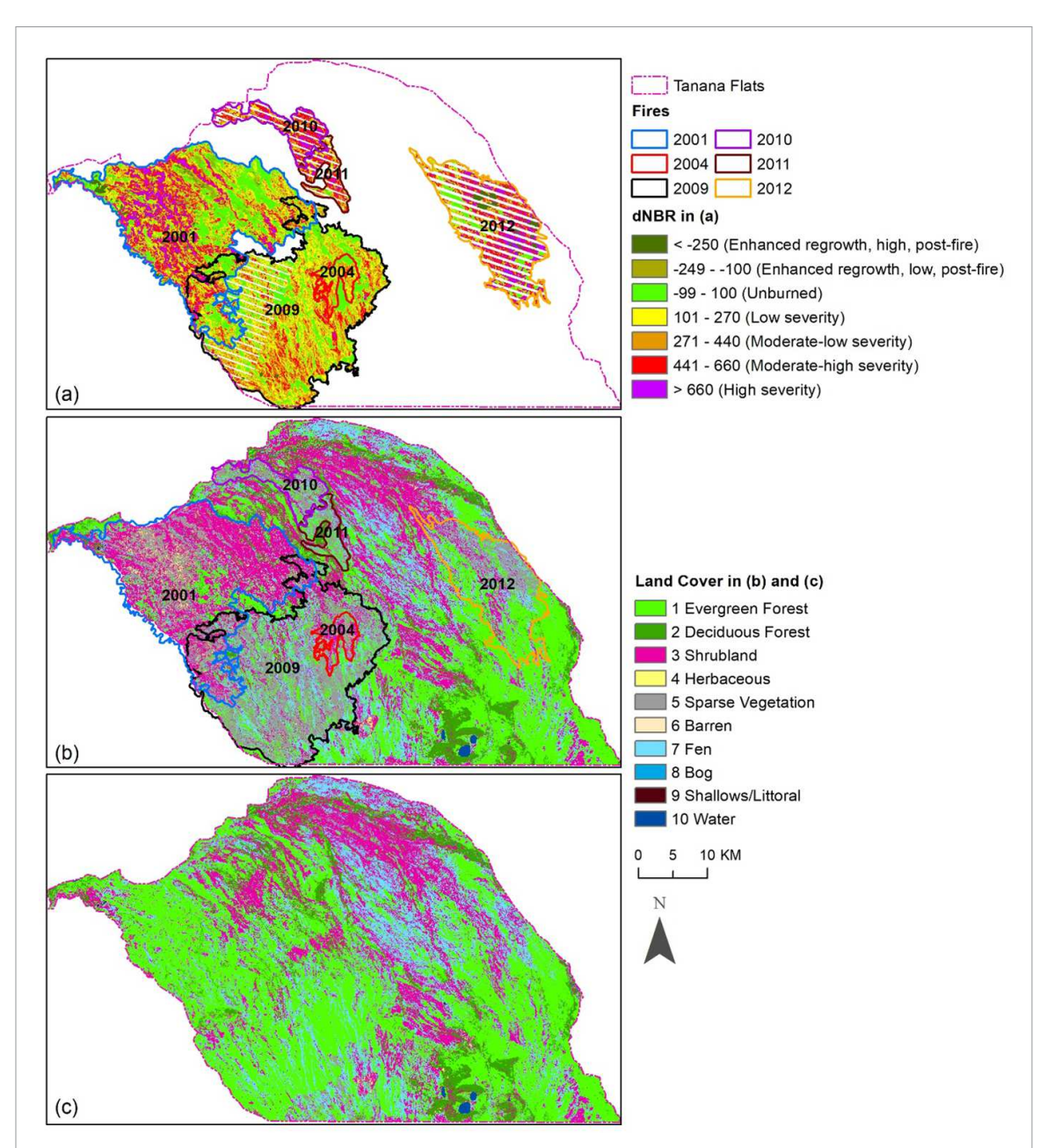


Figure 2. (a) Mosaic of differenced Normalized Burn Ratio (dNBR, scaled by 10³) of six fires and burn severity levels defined by the USGS, and land cover types in (b) 2014 (post-fire), (c) 2000 (pre-fire).

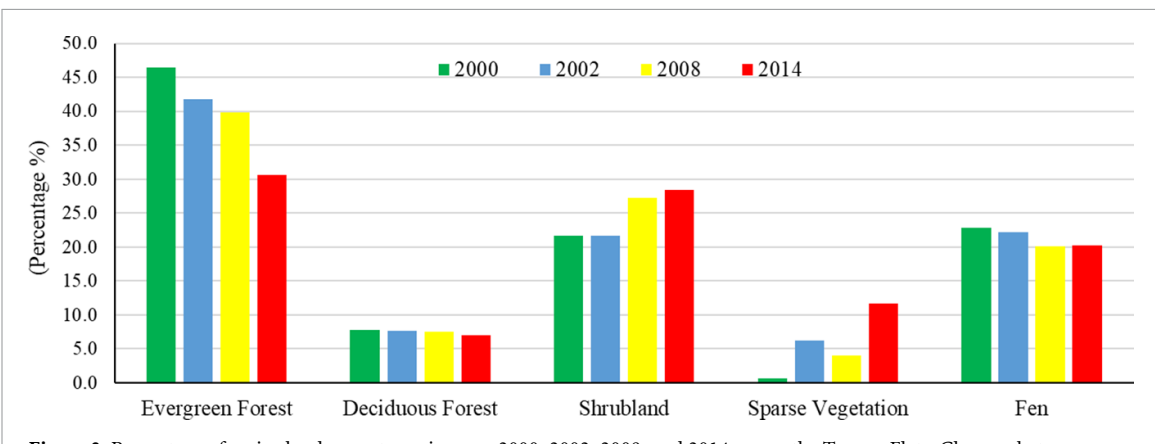


Figure 3. Percentage of major land cover types in years 2000, 2002, 2008, and 2014 across the Tanana Flats. Changes between 2000–2002, 2002–2008, and 2008–2014 were caused by fires in 2001, 2004, and 2009–2012, respectively.

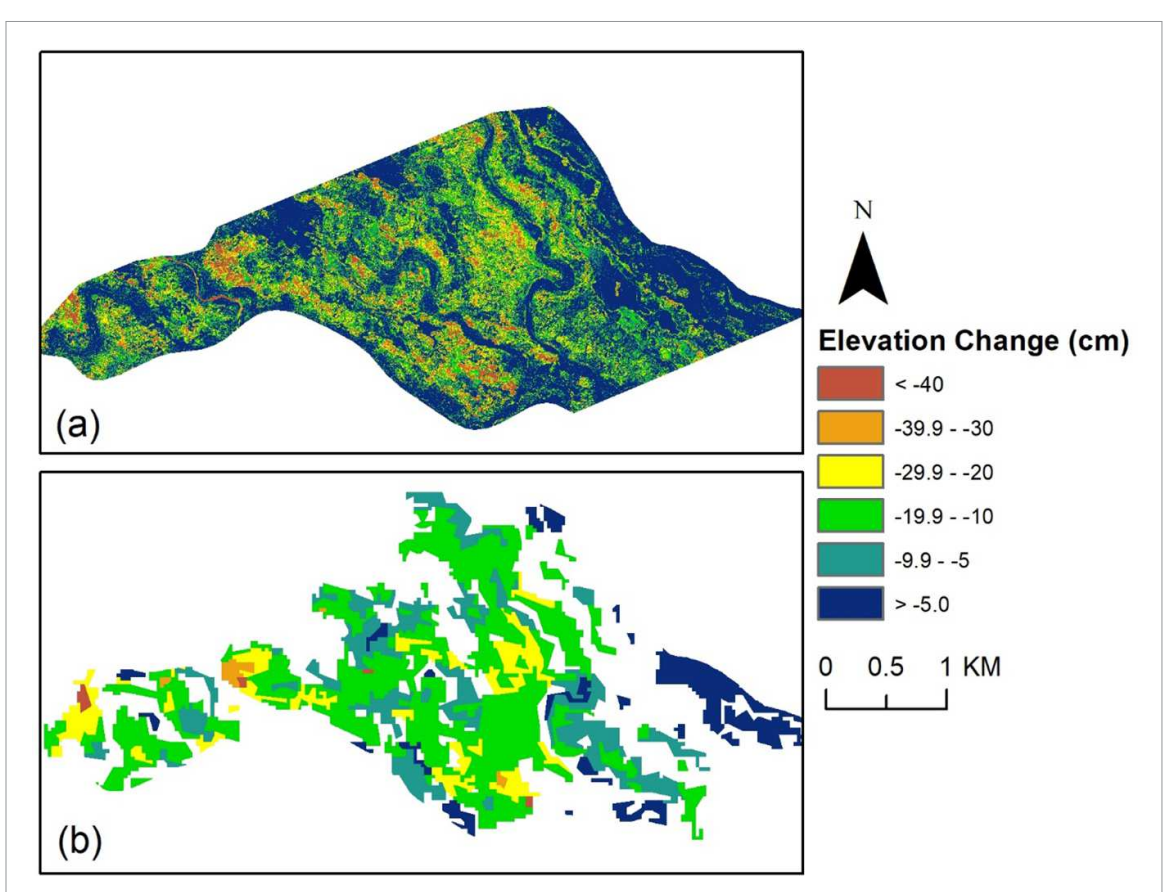


Figure 4. (a) Lidar DoD between 2014 and 2020 before dropping the noise, and (b) detected thaw settlement at the 2010 fire scar after dropping the noise at the object level.

STD of 8.7 cm, a mean decrease of 16.2 cm in deciduous forest with a STD of 5.4 cm, a mean decrease of 19.5 cm in shrubland with a STD of 7.2 cm, and a mean of 20.0 cm in fen with a STD of 16.0 cm in terms of the 2000 land cover types (figure 2(c)). We attribute the consistent elevation decreases in the permafrost-affected evergreen forest, shrubland, and sparse vegetation to thaw settlement, whereas attribute changes in fens to water level changes.

4.2. Model performance, thaw settlement mapping, and analysis

We conducted correlation analyses and applied the variable importance function in the RF algorithm to identify optimal Landsat predictors for thaw settlement. The results illustrated that an inclusion of post-fire NDVI for 1 or 2 years was adequate for thaw settlement estimation, while including timeseries NDVI was not beneficial. Both dNBR and NDVI were valuable for thaw settlement modeling with dNBR negatively related (r = -0.23) and NDVI positively related (0.30-0.4). An addition of NDMI did not improve the model performance due to its high correlation with NDVI. Inclusion of spectral bands 2, 3, 5, and 7 was valuable in the model. Performance of the final selected models with optimal predictors for fire-induced thaw settlement is displayed in table 2. Three machine learning models

Table 2. Model performance for estimating lidar-detected thaw settlement. ANN: artificial neural network; SVM: support vector machine; RF: random forest; EA: ensemble analysis.

	ANN	SVM	RF	EA	
r	0.79	0.81	0.80	0.82	
MAE (cm)	8.3	7.7	7.8	7.1	
RMSE (cm)	11.4	11.0	11.1	10.3	

obtained a comparable result with an r of \sim 0.8, MAE between 7.7 and 8.3 cm, and RMSE within 11.0–11.4 cm. An EA of three machine learning outputs slightly increased the estimation with an r of 0.82, MAE of 7.1 cm and RMSE of 10.3 cm. Analysis of the mean estimation from each model compared to the lidar-detected settlement showed that ANN and SVM underestimated the subsidence while RF overestimated the settlement by less than 1 cm.

We applied the EA model to estimate thaw settlement across all the six fire scars (~1250 km²) on Tanana Flats with a dNBR larger than 100, as shown in figure 5. Thaw settlement within the fire scars was not homogeneous with some regions larger than 25 cm and some areas less than 5 cm. Most of the regions had a settlement larger than 10.0 cm comparable to the RMSE of the EA model, suggesting the model was acceptable. The fire-induced thaw settlement pattern was reasonable by a joint observation of the settlement map (figure 5(a)) and the dNBR map

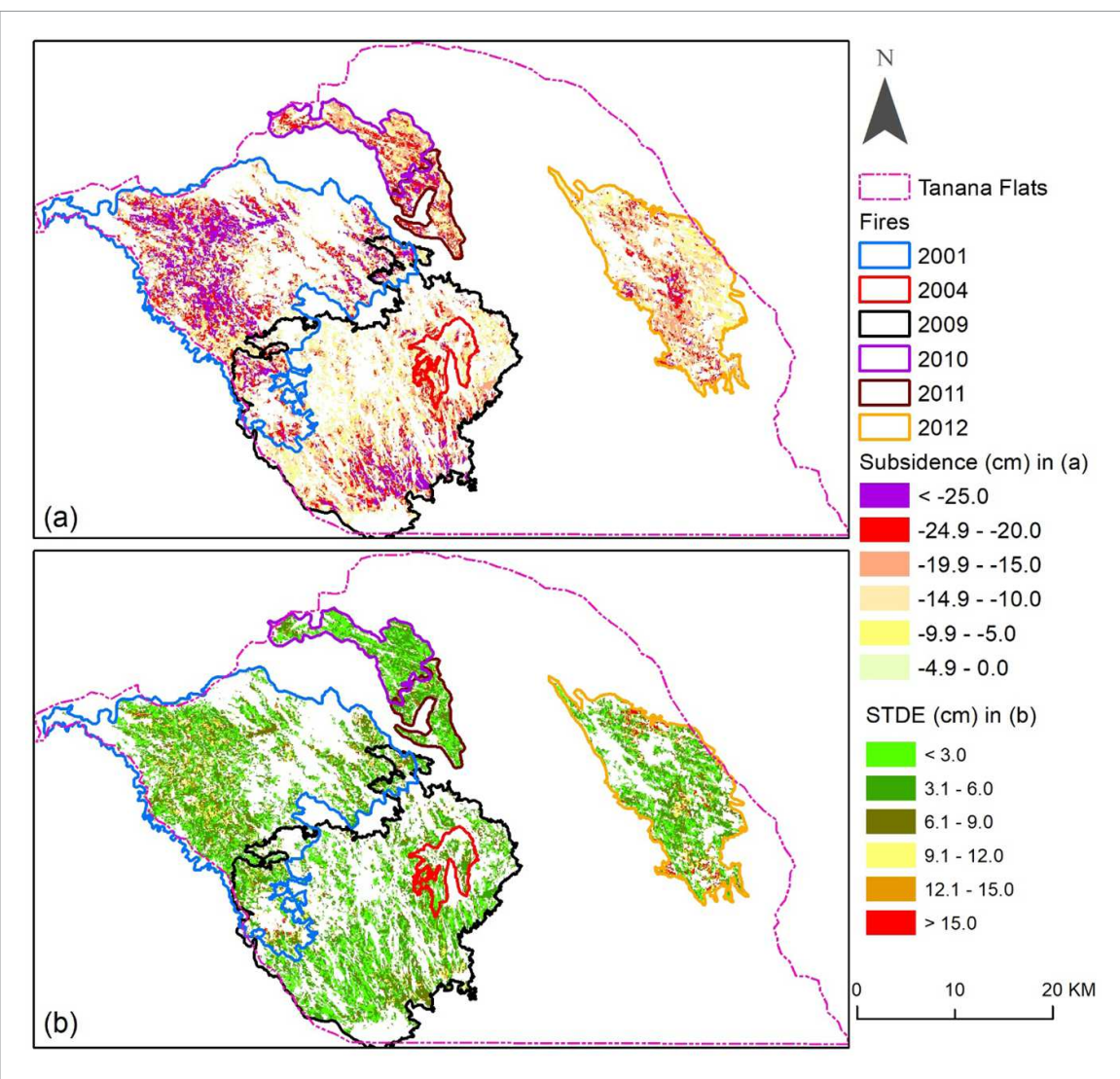


Figure 5. (a) Estimated subsidence (cm) for burned areas (dNBR >100) from the EA; and (b) corresponding STD of multiple model outputs (STDE, cm) from ANN, SVM, and RF.

(figure 2(a)). Severe settlement (<-25 cm, in purple) was mainly present in the 2001 fire and southern part of the 2009 fire due to extensive loss of ecosystem-protection provided by evergreen trees. The STD of multiple model outputs (STDE) map illustrated that three models produced consistent estimations for most areas with STDE less than 6.0 cm (in green in figure 5(b)). A small area in the 2012 fire scar had STDE larger than 15 cm (in red), indicating a large disagreement among the model estimations.

We calculated the mean subsidence across the three major burned vegetation communities evergreen forest, shrubland, and fen, and each fire scar. Areas covered by evergreen forest experienced an averaged subsidence of 17.2 cm, and fen margins had an estimated subsidence of 14.1 cm. Estimated subsidence in Shrubland was 14.1 cm. The across fire analysis revealed that the greatest subsidence occurred in the 2001 fire scar with an estimation of 18.0 cm, which was followed by areas in the 2011 fire scar with an estimation of 17.1 cm. The smallest subsidence was

present in the 2004 fire scar which was reburned in 2009.

5. Discussion

5.1. Effects of wildfire on vegetation and thaw settlement

Fire effects on vegetation on Tanana Flats were generally consistent with findings reported in the boreal and arctic biome following a trajectory of changing evergreen trees to broadleaf trees, shrubs, or grasslands (Li et al 2021). Analyses of the entire ABoVE domain of land cover change during 1984–2014 illustrated that most of the Evergreen Forest loss occurred in localized patches related to fire disturbance (Wang et al 2020). Abrupt decreases in most plant function types caused by burns were also revealed by a recent ABoVE dataset 'Modeled Top Cover by Plant Functional Type over Alaska and Yukon, 1985–2020' (Macander and Nelson 2022, Macander et al 2022). Our time-series analyses of land cover change and

patterns on Tanana Flats across the six fire scars showed a large increase of sparsely vegetated areas in 2002 (post-fire 2001) followed by a large increase of shrubs in 2008 (pre-fire 2009). This particular time span with focus on the 2001 fire scar revealed the path of vegetation shift after fire over this lowland area: a removal of evergreen trees, a transition of sparsely vegetated area, and then a colonization of shrubs. Further observation of the land cover maps of 2000 (prefire) (figure 2(c)) and 2014 (post-fire) (figure 2(b)) showed that the expansion of shrubs to sparsely vegetated areas started from areas occupied by fens which became shrubbier after fire. We found that fens could also expand into burned shrubs. A shrub-rich fen system was favorably developed due to the association of fens and shrubs in the fire regime at the lowland Tanana Flats. However, most severely burned areas were still classified as the sparse vegetation mixed with herbaceous in the 2014 land cover map, suggesting it might take more than two decades for a complete colonization of shrubs over these areas. Similar shifting patterns are underway for burned areas caused by fires between 2009 and 2012, although a distinct expansion of shrubs toward fens and sparsely vegetated areas has not been observed in the 2014 land cover map across these scars. The fire and climate warming induced expansion of shrubs often occurs in tundra areas (Myers-Smith and Hik 2017), but the rapid regeneration of shrubs following fires is also reported in interior Alaska (Jorgenson et al 2013). Our field visits showed an abundant spruce and birch regeneration at the fire scars of 2001 and 2010, but it was very slow. It could take decades for this to be visible on Landsat imagery. Failure of regeneration is possible because a synthesis study from Baltzer et al (2021) showed that interior Alaska had the highest instances of total regeneration failure of any tree species after a fire based on 1538 field sites across boreal North America. Earlier aerial photographybased maps during 1949-1995 revealed a large shift from broadleaf birch to fens and bogs due to climate warming, leading to a widespread permafrost degradation on Tanana Flats (Jorgenson et al 2013). In terms of our land cover maps, deciduous forest (birch) now only accounts for 7%. Fires are accelerating the elimination of lowland birch forests over this area. The recovery of vegetation-permafrost may take decades and is unlikely to return its pre-burn conditions under a warming climate scenario.

Effects of fire on permafrost thaw and surface settlement is complicated by the interaction of numerous biophysical factors, including highly variable ground ice contents (Jorgenson *et al* 2013), fire severity (Gibson *et al* 2018), surface vegetation (Van Cleve and Viereck 1983), changes in soil organic thickness (Nossov *et al* 2013, Gibson *et al* 2018), hydrology and lateral degradation (Kurylyk *et al* 2016, Douglas *et al* 2021), depth of snowpack (Douglas and Zhang 2021), and climate (Jorgenson *et al* 2022). On the Tanana

Flats, volumetric ice contents in the top 3 m often vary from 40% to 80% (Jorgenson *et al* 2001) and thaw settlement up to 50 cm was observed within a few years after the 2010 fire (Brown *et al* 2015). In our analysis, elevation decreases were spatially variable. Given the close association of field and lidar measurements of elevation changes (Brown *et al* 2015), we are confident in concluding that the large elevation decrease is due to permafrost thaw after fire and subsequent thaw settlement.

5.2. Capacity of Landsat products for quantifying fire-induced thaw settlement

This study shows there is a strong relationship between fire-induced thaw settlement and Landsat observations. A combination of Landsat reflectance, NDVI, and burn severity dNBR could explain \sim 65% variance of lidar-detected thaw settlement. The fire severity dNBR was the most critical factor in controlling the settlement based on the function of variable importance to measure the contribution of each variable in the RF algorithm, similar to what was observed by Jones et al (2015). Landsat spectral reflectance band 2 (blue) was the second important factor in the estimation, because it is valuable for distinguishing soil from vegetation (USGS 2022). The addition of band 2 was useful because of the large exposure of bare lands, and expansion of deciduous vegetation after fire. NDVI was the third important variable in the estimation. Analyses of time-series NDVI after fire, as well as other spectral indices such as NBR, can indicate the recovery of greenness and vegetation regrowth (Pérez-Cabello et al 2021). Thus, inclusion of NDVI was useful in the estimation. However, an addition of time series NDVI was not beneficial. We observed a consistent increase of NDVI across time (2013-2021) within each fire scar. This trend did not contribute the estimation of thaw settlement. Including one or two NDVIs in the model was adequate to characterize the response of plants across space and time, and its covariation with fire-induced thaw settlement. Inclusion of band 5 (near infrared) and band 7 (shortwave infrared) also improved the estimation in the ANN model but was not valuable in the RF model. To be consistent, we included both bands in the modeling and final estimation.

5.3. Object-based machine learning ensemble estimation

Application of machine learning for fire-induced thaw settlement modeling was valuable. Three machine learning algorithms ANN, SVM and RF achieved a comparable performance in the model in terms of the matched dataset, but the estimations for mapping were different. These differences were expected due to differences in the architecture of the algorithms. ANN models data as a structure of neurons and synapses of human brains. SVM looks for an optimal hyperplane to minimize training errors,

whereas RF searches for optimal decision trees to generalize a model. Due to the weaknesses and strengths of each algorithm, an EA of multiple model outputs can make the estimation more robust than the application of an individual model alone. This is especially critical for regions without any field or lidar measurements but with a high diversity in prediction from models. Furthermore, an application of ensemble estimation generated an uncertainty map (figure 5(b)) to complement traditional performance metrics. This map reveals the uncertainty based on model analyses and identify regions with varying confidence in prediction. This type of map can guide field or lidar data collection for further validations, preferably over regions where large differences in model estimations were obtained.

The object-based modeling and mapping was beneficial. Lidar DEMs often have a high spatial resolution (<5 m) while Landsat has a moderate spatial resolution (30 m). Resampling lidar DEMs into 30 m to match Landsat would bring uncertainties from the resampling algorithms though this resampling may reduce some uncertainties from lidar measurements. Matching lidar data and Landsat at the object level was more reasonable by segmenting the Landsat imagery into relatively homogeneous patches and calculating the mean subsidence within each patch detected by repeat lidar to develop the model and estimate subsidence. In addition, application of the mean lidar-detected thaw settlement for a patch could filter out a portion of errors from lidar measurements. We did not examine the pixel-based matching and modeling in this study, but detailed comparison between pixel-based and object-based modeling and mapping for estimating wetland soil properties was provided in Zhang et al (2019).

5.4. Limitations and sources of error

Constraints in applied datasets and data processing and analyses were identified as two major sources of limitations and errors in this study. First, there was a time gap between the occurrence of fire and lidar data collection. The overlapped area between repeat lidar and the latest fire was the 2010 fire where the first lidar was collected in 2014 (4 year time gap). Field data analyses between 2011 and 2014 in the forests burned in 2010 showed that the subsidence was up to 50 cm (Brown et al 2015). This suggests that an addition of up to \sim 50 cm should be added to the lidar-detected subsidence across the burned forests, or the final projection from our model. Our estimated thaw settlement across the 2010 fire was \sim 15.5 cm, indicating a decreasing rate of thaw settlement during 2014-2020 with the recovery of vegetation. The total fire-induced thaw settlement for the burned forests could be up to \sim 60–70 cm if lidar data were collected in 2011. Field measurements revealed an average of ground elevation change of \sim 27 cm along a transect in the 2010 fire scar (Brown et al 2015), suggesting subsidence

was smaller for other plant communities. This was consistent with the lower subsidence estimated in our study.

Second, the repeat lidar measurements in the 2010 fire scar had a small coverage (~10 km², figure 4) in terms the scars of six fires (\sim 1250 km²) to be mapped. Evergreen forest, deciduous forest, shrubland and fen were present in the lidar coverage with varying burn severity, however, only limited training samples were obtained, especially for deciduous forest (~0.06 km²). Repeat lidar or field measurements across all fire scars using a sampling scheme would generate a better estimation but in practice collecting such type of data is challenging or costly, especially in a remote area like Tanana Flats. Limited lidar data coverage was identified as a major error source in the estimation. The in-orbit Ice, Cloud, and land Elevation Satellite 2 (ICESat-2) has potential for large scale elevation change analyses with a revisit of 91 d (Michaelides et al 2021), but it has a coarse spatial resolution, worse precision, as well as other issues compared to airborne repeat lidar. An integrated application of airborne lidar, ICESat-2, InSAR and Landsat data products may improve the thaw settlement estimation given the complementary features of each sensor system. This was identified as the future research need.

The third constraint was from Landsat products. There might be more uncertainties using Landsat 8 for predicting the thaw settlement for the 2001 fire due to the large time gap between this fire and Landsat 8 products. Ideally, for the 2001 estimation, Landsat products within 4 years following the fire should be used. However, direct application of Landsat 5 products for the 2001 fire generated a poor pattern (results were not shown) due to the difference of reflectance and NDVI across sensors (Roy et al 2016, Berner et al 2020). Cross-calibration models have been developed to address this issue, but it involves more data preprocessing. Snow and cloud cover is another issue using Landsat products as well as other spaceborne optical sensors. For interior Alaska, snow free imagery is limited to a time window between May and September, and the need for cloud free conditions further constrain data availability for such applications.

The fourth constraint came from the incompleteness of predictors in the machine learning model in relation to the factors affecting thaw settlement. Despite the complicated biophysical interactions that affect permafrost thaw and surface settlement, Landsat products explained 65% of the variance in lidar-detected thaw settlement but the models did not capture all drivers controlling thaw subsidence. Time since disturbance is particularly important because thaw is more rapid immediately after disturbance, slows with time, and can continue over many decades (Burn 1998). Inclusion of soil variables, particularly ground ice contents, or others might increase the

estimation, but such types of data products with comparable resolution to Landsat are often not available.

Data processing and analysis is the last major source of error. Though the developed object-based machine learning ensemble approach was encouraging for thaw settlement estimation, uncertainties from major processing steps like image segmentation and parameters used in machine learning were inevitable. An evaluation of the selected processing techniques for estimating settlement was beyond this study but was identified as an area of future research need. An independent subsidence dataset such as InSAR or ICESat-2 estimation was also needed to further evaluate the Landsat estimated settlement. The upcoming NASA-Indian Space Research Organization Synthetic Aperture Radar mission to be launched in 2024 would offer another opportunity to validate the settlement estimation at a broad coverage.

6. Summary and conclusions

We systematically evaluated the effects of six large fires on the ice-rich Tanana Flats lowland in interior Alaska and for the first time estimated and mapped fire-influenced thaw settlement over ~1250 km². In total the six fires resulted in a loss of ~400 km² evergreen forest during 2000–2014 among ~590 km² fire-influenced forests with varying degree of burn severity. The fires provided favorable conditions for shrub-fen development, resulting in a comparable post-fire coverage of shrubland and evergreen forest and increasing encroachment of shrubland to areas with sparse vegetation. The regrowth of forests was not observed after 13 years of the oldest fire 2001 based on Landsat observations.

Despite of uncertainties in the timing of lidar data acquisition following a wildfire, we generated a reasonable fire-induced thaw settlement pattern which was generally consistent with the burn severity pattern. Our study indicated that linking airborne repeat lidar with Landsat products was an encouraging tool for large scale quantification of fire-induced thaw settlement. While there are no constraints to applying this methodology to other fire-influenced permafrost terrains, direct application of our developed model to other boreal or tundra areas is limited because the model was calibrated by site-specific lidar measurements, and ice contents and thaw settlement potential is highly variable among terrain types. Because airborne lidar measurements are increasingly being made across northern permafrost regions (e.g. Jones et al 2015, Rodenhizer et al 2022), our method is a valuable means of projecting elevation change across entire fire scars within uniform permafrost-affected landscapes by using data-driven machine learning techniques. Our approach is complementary to the application of InSAR (e.g. Yanagiya and Furuya 2020) or lidar technique alone (e.g. Jones et al 2015) for thaw subsidence estimations. Its ability to combine active

airborne lidar sensors with passive spaceborne optical sensors for a large-scale quantification of fire-induced thaw settlement is unique. It is anticipated that this work can advance the multi-sensor fusion techniques for permafrost thawing studies under the scenario of climate warming and increasing fire activities in cold regions.

Data availability statement

The data that support the findings of this study are available upon reasonable request from the authors.

Acknowledgments

This research was funded by the U S Army Corps of Engineers (USACE) Engineer Research and Development Center Applied Research Program Office for Installations and Operational Environment and Basic Research Program under PE 0601102/AB2 (Protection, Maneuver, Geospatial, Natural Sciences), the Department of Defense's Strategic Environmental Research and Development Program (Projects RC-2110 and RC18-1170), and the U S Department of Energy, Office of Science, Environmental System Science program (under 0000260300). We acknowledge datasets and collaboration with NASA's Arctic-Boreal Vulnerability Experiment (ABoVE).

ORCID iDs

Caiyun Zhang https://orcid.org/0000-0002-6603-0427

Thomas A Douglas https://orcid.org/0000-0003-1314-1905

David Brodylo https://orcid.org/0000-0002-0331-2398

References

Anders K, Marx S, Boike J, Herfort B, Wilcox E J, Langer M, Marsh P and Höfle B 2020 Multitemporal terrestrial laser scanning point clouds for thaw subsidence observation at Arctic permafrost monitoring sites *Earth Surf. Process. Landf.* 45 1589–600

Anguita D, Ghelardoni L, Ghio A, Oneto L and Ridella S, 2012 The 'K' in K-fold cross validation ESANN 2012 Proc. European Symp. on Artificial Neural Networks Computational Intelligence and Machine Learning Bruges, Belgium April pp 25–27

Antonova S, Sudhaus H, Strozzi T, Zwieback S, Kääb A, Heim B, Langer M, Bornemann N and Boike J 2018 Thaw subsidence of a yedoma landscape in northern Siberia, measured *in situ* and estimated from TerraSAR-X interferometry *Remote* Sens. 10 1–27

Baltzer J L *et al* 2021 Increasing fire and the decline of fire adapted black spruce in the boreal forest *Proc. Natl Acad. Sci. USA* 118 e2024872118

Belgiu M and Drãguţ L 2016 Random forest in remote sensing: a review of applications and future directions *ISPRS J. Photogramm. Remote Sens.* 114 24–31

Berner L T *et al* 2020 Summer warming explains widespread but not uniform greening in the Arctic tundra biome *Nat*. *Commun.* 11 4621

- Bhardwaj A, Samb L, Bhardwaj A and Martín-Torres J 2016 Lidar remote sensing of the cryosphere: present applications and future prospects Remote Sens. Environ. 177 125–43
- Breiman L 2001 Random forests Mach. Learn. 45 5-32
- Brown D R N, Jorgenson M T, Douglas T A, Romanovsky V E, Kielland K, Hiemstra C, Euskirchen E S and Ruess R W 2015 Interactive effects of wildfire and climate on permafrost degradation in Alaskan lowland forests J. Geophys. Res. Biogeosci. 120 1619–37
- Burn C R 1998 The response (1958–1997) of permafrost and near-surface ground temperatures to forest fire, Takhini River valley, southern Yukon Territory *Can. J. Earth Sci.* 35 184–99
- Chasmer L and Hopkinson C 2017 Threshold loss of discontinuous permafrost and landscape evolution Glob. Change Biol. 23 2672–86
- Dong P and Chen Q 2018 Lidar Remote Sensing and Applications (Boca Raton, FL: CRC Press)
- Douglas T A et al 2021 Recent degradation of interior Alaska permafrost mapped with ground surveys, geophysics, deep drilling, and repeat airborne lidar Cryosphere 15 3555–75
- Douglas T A, Jones M C, Hiemstra C A, Arnold J R and Blum J D 2014 Sources and sinks of carbon in boreal ecosystems of interior Alaska: a review *Elementa* 2 000032
- Douglas T A, Jorgenson M T, Brown D R N, Campbell S W, Hiemstra C A, Saari S P, Bjella K and Liljedahl A K 2015 Degrading permafrost mapped with electrical resistivity tomography, airborne imagery and lidar, and seasonal thaw measurements *Geophysics* 81 WA71–85
- Douglas T A and Zhang C 2021 Machine learning analyses of remote sensing measurements establish strong relationships between vegetation and snow depth in the boreal forest of interior Alaska *Environ. Res. Lett.* **16** 065014
- Dramsch J S 2020 70 years of machine learning in geoscience in review *Adv. Geophys.* **61** 1–88
- Dronova I 2015 Object-based image analysis in wetland research: a review *Remote Sens.* 7 6380–413
- Flood N 2014 Continuity of reflectance data between Landsat-7 ETM+ and Landsat-8 OLI, for both top-of-atmosphere and surface reflectance: a study in the Australian landscape Remote Sens. 16 7952–70
- Gibson C M, Chasmer L E, Thompson D K, Quinton W L, Flannigan M D and Olefeldt D 2018 Wildfire as a major driver of recent permafrost thaw in boreal peatlands Nat. Commun. 9 3041
- Goetz S *et al* 2022 An overview of NASA's Arctic Boreal Vulnerability Experiment (ABoVE): development, implementation, advances and knowledge gaps *Environ. Res.* Lett. accepted
- Hall M, Frank E, Holmes G, Pfahringer B, Reutemann P and Witten I H 2009 The WEKA data mining software: an update *SIGKDD Explorations* 11 10–18
- Holloway J E, Lewkowicz A G, Douglas T A, Li X, Turetsky M R, Baltzer J and Jin H 2020 Impact of wildfire on permafrost landscapes: a review of recent advances and future prospects Permafr. Periglac. Process. 31 371–82
- Jones B M, Grosse G, Arp C D, Miller E, Liu L, Hayes D J and Larsen C F 2015 Recent Arctic tundra fire initiates widespread thermokarst development Sci. Rep. 5 15865
- Jones B M, Stoker J M, Gibbs A E, Grosse G, Romanovsky V E, Douglas T A, Kinsman N E M and Richmond B M 2013 Quantifying landscape change in an arctic coastal lowland using repeat airborne lidar *Environ. Res. Lett.* 8 045025
- Jorgenson M T et al 2013 Reorganization of vegetation, hydrology and soil carbon after permafrost degradation across heterogeneous boreal landscapes Environ. Res. Lett. 8 035017
- Jorgenson M T, Brown D, Hiemstra C A, Genet H, Marcot B G, Murphy R G and Douglas T A 2022 Drivers of historical and

- projected changes in diverse boreal ecosystems: fires, thermokarst, riverine dynamics, and humans *Environ. Res.*
- Jorgenson M T, Douglas T A, Liljedahl A K, Roth J E, Cater T C, Davis W A, Frost G V, Miller P F and Racine C H 2020 The roles of climate extremes, ecological succession, and hydrology in repeated permafrost aggradation and degradation in fens on the Tanana Flats, Alaska *J. Geophys. Res. Biogeosci.* 125 e2020JG005824
- Jorgenson M T, Racine C H, Walters J C and Osterkamp T E 2001 Permafrost degradation and ecological changes associated with a warming climate in central Alaska Clim. Change 48 551–79
- Jorgenson M T, Romanovsky V, Harden J, Shur Y, O'Donnell J, Schuur E A G, Kanevskiy M and Marchenko S 2010 Resilience and vulnerability of permafrost to climate change Can. J. For. Res. 40 1219–36
- Jorgenson M T, Roth J E, Raynolds M K, Smith M D, Lentz W, Zusi-Cobb A L and Racine C H 1999 An ecological land survey for Fort Wainwright *CRREL Report 99-9* (Alaska: U.S. Army Cold Regions Research and Engineering Laboratory) p 83
- Keeley J E 2009 Fire intensity, fire severity and burn severity: a brief review and suggested usage *Int. J. Wildland Fire* 18 116–26
- Kurylyk B L, Hayashi M, Quinton W L, McKenzie J M and Voss C I 2016 Influence of vertical and lateral heat transfer on permafrost thaw, peatland landscape transition, and groundwater flow Water Resour. Res. 52 1286–305
- Li X Y et al 2021 Influences of forest fires on the permafrost environment: a review Adv. Clim. Change Res. 12 48–65
- Liu L, Jafarov E E, Schaefer K M, Jones B M, Zebker H A, Williams C A, Rogan J and Zhang T 2014 InSAR detects increase in surface subsidence caused by an Arctic tundra fire Geophys. Res. Lett. 41 3906–13
- Loboda T V, Chen D, Hall J V and He J 2018 ABoVE: Landsat-derived Burn Scar dNBR across Alaska and Canada, 1985–2015 (Oak Ridge, TN: ORNL DAAC)
- Macander M J and Nelson P R 2022 ABoVE: Modeled Top Cover by Plant Functional Type over Alaska and Yukon, 1985–2020 (Oak Ridge, TN: ORNL DAAC) (https://doi.org/ 10.3334/ORNLDAAC/2032)
- Macander M J, Nelson P R, Nawrocki T W, Frost G V,
 Orndahl K M, Palm E C, Wells A F and Goetz S J 2022
 Time-series maps reveal widespread change in plant
 functional type cover across Arctic and boreal Alaska and
 Yukon Environ. Res. Lett. 17 054042
- Mas J F and Flores J J 2008 The application of artificial neural networks to the analysis of remotely sensed data *Int. J. Remote Sens.* **29** 617–63
- Michaelides R J, Bryant M B, Siegfried M R and Borsa A A 2021 Quantifying surface-height change over a periglacial environment with ICESat-2 laser altimetry *Earth Space Sci.* 8 e2020EA001538
- Michaelides R J, Schaefer K, Zebker H A, Parsekian A, Liu L, Chen J, Natali S, Ludwig S and Schaefer S R 2019 Inference of the impact of wildfire on permafrost and active layer thickness in a discontinuous permafrost region using the remotely sensed active layer thickness (ReSALT) algorithm *Environ. Res. Lett.* 14 035007
- Minsley B J, Pastick N J, Wylie B K, Brown D R N and Kass M 2016 Evidence for nonuniform permafrost degradation after fire in boreal landscapes *J. Geophys. Res. Earth Surf.* 121 320–35
- Molan Y E, Kim J W, Lu Z, Wylie B and Zhu Z 2018 Modeling wildfire-induced permafrost deformation in an Alaskan boreal forest using InSAR observations *Remote Sens.* **10** 405
- Mountrakis G, Im J and Ogole C 2011 SVMs in remote sensing: a review *ISPRS J. Photogramm. Remote Sens.* **66** 247–59

- Myers-Smith I H and Hik D S 2017 Climate warming as a driver of tundra shrubline advance *J. Ecol.* **106** 547–60
- Nossov D R, Jorgenson M T, Kielland K and Kanevskiy M Z 2013 Edaphic and microclimatic controls over permafrost response to fire in interior Alaska *Environ. Res. Lett.* 8 035013
- Pérez-Cabello F, Montorio R and Alves D B 2021 Remote sensing techniques to assess post-fire vegetation recovery Curr. Opin. Environ. Sci. Health 21 100251
- Rodenhizer H, Belshe F, Celis G, Ledman J, Mauritz M, Goetz S, Sankey T and Schuur E A G 2022 Abrupt permafrost thaw accelerates carbon dioxide and methane release at a tussock tundra site Arct. Antarct. Alp. Res. 54 443–64
- Roy D P, Kovalskyy V, Zhang H K, Vermote E F, Yan L, Kumar S S and Egorov A 2016 Characterization of Landsat-7 to Landsat-8 reflective wavelength and normalized difference vegetation index continuity *Remote Sens. Environ.* **185** 57–70
- Sun Z et al 2022 A review of Earth Artificial Intelligence Comput. Geosci. 159 105034
- Trimble 2020 eCognition Developer 10.0 Reference Book (Munich: Trimble Germany GmbH)
- USGS 2022 What are the best Landsat spectral bands for use in my research? (available at: www.usgs.gov/faqs/what-are-best-landsat-spectral-bands-use-my-research) (Accessed 9 June 2022)
- Van Cleve K and Viereck L A 1983 A comparison of successional sequences following fire on permafrost-dominated and permafrost-free sites in interior Alaska Proc. 4th Int. Conf. on Permafrost (Fairbanks, AK: National Academy Press) pp 1286–91
- Vapnik V N 1995 *The Nature of Statistical Learning Theory* (New York: Springer)

- Wang J A, Sulla-Menashe D, Woodcock C E, Sonnentag O, Keeling R F and Friedl M A 2019 ABoVE: Landsat-derived annual dominant land cover across ABoVE core domain, 1984–2014 ORNL DAAC (Oak Ridge, TN)
- Wang J A, Sulla-Menashe D, Woodcock C E, Sonnentag O, Keeling R F and Friedl M A 2020 Extensive land cover change across Arctic–Boreal northwestern North America from disturbance and climate forcing Glob. Change Biol. 26 807–22
- Wheaton J M, Brasington J, Darby S E and Sear D A 2010 Accounting for uncertainty in DEMs from repeat topographic surveys: improved sediment budgets *Earth Surf. Process. Landf.* 35 136–56
- Yanagiya K and Furuya M 2020 Post-wildfire surface deformation near Batagay, Eastern Siberia, detected by L-band and C-band InSAR *J. Geophys. Res. Earth. Surf.* 125 e2019JF005473
- Zhang C, Brodylo D, Rahman M, Rahman M A, Douglas T A and Comas X 2022 Using an object-based machine learning ensemble approach to upscale evapotranspiration measured from eddy covariance towers in a subtropical wetland *Sci. Total Environ.* **831** 154969
- Zhang C, Denka S, Cooper H and Mishra D R 2018 Quantification of sawgrass marsh aboveground biomass in the coastal Everglades using object-based ensemble analysis and Landsat data Remote Sens. Environ. 204 366–79
- Zhang C, Douglas T A and Anderson J 2021 Modeling and mapping permafrost active layer thickness using field measurements and remote sensing techniques Int. J. Appl. Earth Obs. Geoinf. 102 102455
- Zhang C, Mishra D R and Pennings S 2019 Mapping salt marsh soil properties using imaging spectroscopy *ISPRS J. Photogramm. Remote Sens.* **148** 221–34